https://doi.org/10.1016/j.neucom.2018.04.066

A general memristor-based pulse coupled neural network with variable linking coefficient for multi-focus image fusion

Zhekang Dong [a,b] , Chun Sing Lai [b,c,d], Donglian Qi [a*], Zhao Xu [b], Chaoyong Li [a], Shukai Duan [e]

[a] *College of Electrical Engineering, Zhejiang University, Hangzhou 310027, China*
[b] *Department of Electrical Engineering, The Hong Kong Polytechnic University, Hong Kong, China*
[c] *Department of Engineering Science, University of Oxford, 17 Parks Road, Oxford OX1 3PJ, United Kingdom*
[d] *Department of Electrical Engineering, School of Automation, Guangdong University of Technology, Guangzhou 510006, China*
[e] *School of Electronic and Information Engineering, Southwest University, Chongqing 310027, China*

Abstract

Pulse coupled neural network (PCNN) is a kind of visual cortex-inspired biological neural network, which has been proved a powerful candidate in the field of digital image processing due to its unique characteristics of global coupling and pulse synchronization. Notably, the inherent parameters estimation issue emerging in the entire system greatly affects the overall network performance. In this paper, a novel memristor crossbar array with its corresponding peripheral circuits is proposed, which is able to construct a general memristor-based PCNN (MPCNN) with variable linking coefficient. In order to verify the effectiveness and generality of the presented network, the single-channel MPCNN is further applied into the multi-focus image fusion problem with an improved multi-channel configuration. Correspondingly, a new type of MPCNN-based image fusion algorithm is put forward along with the design of an appropriate mapping function based on the image orientation information measure. Finally, a series of contrast experiments with comprehensive analysis demonstrate that the proposed fusion method has superior performances in terms of image quality and fusion effect compared to several existing algorithms.

Keywords: Pulse coupled neural network, parameters estimation issue, memristor crossbar array, multi-focus image fusion

1. Introduction

The pulse coupled neural network (PCNN) was originally developed by Eckhorn in 1990 based on the experimental observations of synchronous pulse bursts in cat and monkey visual cortex [1, 2]. As a biologically inspired neural network model, the PCNN possesses numerous unique properties including pulse coupling, pulse synchronization, multiplication modulation and variable threshold [1-3], which makes it an efficient alternative in the field of image processing, such as image enhancement [4, 5], image segmentation [6, 7], image denoising [8, 9], object and edge detection [10, 11], image fusion [12-16], and so forth. While the PCNN is definitely a parameter-controlled network system [3], the network parameters estimation issue has been considered as a significant factor affecting the overall performance of all the aforementioned PCNN-based image processing applications. Correspondingly, an appropriate remedy for addressing this inherent limitation is to constitute an adaptive PCNN model with flexible network parameters. However, compared with the PCNN-based application research, little work is explored about the establishment of the parameter-adaptive PCNN model itself. Take the linking coefficient for example, this parameter represents the connection strength among the neurons in PCNN and plays a key role in the specific dynamic behaviors (including pulse statistical characteristics, synchronous oscillation, and pulse transmission attribute [1-3]). Based on this, Li et al. present an adaptive parameters determination strategy to obtain the value of linking coefficient and realize the image segmentation task successfully [6]. In [12], the linking coefficient variation totally depends on the clarity of the input stimuli, which is beneficial for making full use of the surrounding information and achieving good image fusion effect. Similarly, the published literature [16] utilized the average gradient of each pixel as the linking coefficient for the implementation of the infrared and visible image fusion. Notably, all these above-mentioned adaptive parameter setting methods are realized by program simulation on computer, which may lead to the issues in terms of time consuming and low efficiency. Hence, the requirement for hardware implementation of adaptive parameters in PCNN is urgent and necessary.

Fortunately, the recent advent of nanoscale memristors [17, 18] has opened up the potential to address the parameter estimation problem occurred in the existing PCNN models. The memristor was first theorized as a passive electrical element, which provides the ever-missing link between the electric charge and magnetic flux [17, 18]. On account of the advantages of nanoscale geometries, variable conductivity and nonvolatility, the memristor and relevant composite circuits have been demonstrated effective in many applications, including signal processing [19-21], neuromorphic system [22-24], pattern

---

Corresponding email: qidl@zju.edu.cn (D. Qi).

recognition [25-27], nonvolatile memory [28-30], etc. Particularly, the memristor crossbar array with compact construction and high-speed parallel processing capability is indeed an ideal option for realizing the large-scale information processing and adaptive neural network [31-33]. Hence, in this paper, a specific construction strategy for the implementation of the memristor-based PCNN (MPCNN) with adjustable parameter (primarily refers to the linking coefficient) is investigated, and the main contributions are briefly concluded as follows:

1). A novel memristor-based circuit with crossbar array configuration is designed to realize the self-adjustment linking coefficient in PCNN, which is expected to promote the hardware implementation of the adaptive PCNN model with advantages in integration scale reduction, low energy consumption, and high processing efficiency.

2). During the entire establishment process of the MPCNN, the design of the mapping function can be flexible and diverse, which keeps the general MPCNN model in the optimal network state for different applications.

3). For the sake of verification, the presented MPCNN is further applied to the multi-focus image fusion problem. The contrast experiments demonstrate that the MPCNN-based fusion method is not only able to achieve a satisfactory fusion result both in the visual effect and the objective assessment, but also fill the gaps related to the parameter estimation and efficiency enhancement.

4). The entire scheme provides a novel path for implementing PCNN-based applications on the hardware platform, instead of program simulations on computer.

The outline of the paper is organized as follows. Section 2 describes the TiO_2/TiO_{2-x} memristor model and its basic characteristics with formula derivation. Section 3 briefly reviews the classical PCNN model and provides the hardware implementation scheme of the adaptive linking coefficient in PCNN. Following that, the relevant multi-focus image fusion strategy is investigated in Section 4. Furthermore, several contrast experiments with the comprehensive analysis are conducted to illustrate the superiority of the presented algorithm in Section 5. Finally, Section 6 concludes the entire work.

2. Memristor basics

Memristor is a nonlinear circuit element satisfying Ohm's law with a time-varying resistance $M(t)$ whose value depends on the amount of the charge or flux flowing through it [17, 18]. Among the various memristor models, Hewlett Packard (HP) TiO_2 / TiO_{2-x} memristor (as shown in Fig. 1) is one of the most widely used models owing to its simple physical configuration and mathematical expression.

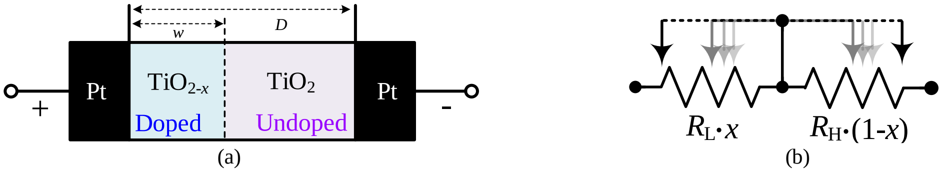

Fig. 1: The HP TiO_2 / TiO_{2-x} memristor. (a) The physical model of HP memristor. (b) The corresponding equivalent circuit

Actually, this device can be deemed as a thin TiO_2 double-layer structure with the total width of D sandwiched between a pair of platinum (Pt) electrodes. Specifically, the oxygen-deficient layer TiO_{2-x} with high conductivity is defined as the doped region, while the other layer TiO_2 with insulating property is named as the undoped region. A voltage applied to the device can drive the doping front between these two layers, and the resistance variation of the memristor can be achieved. Then, the overall resistance of HP memristor, i.e., memristance $M(t)$, can be mathematically expressed by

$$\begin{gathered} M(t) = R_{\mathrm{H}} + (R_{\mathrm{L}} - R_{\mathrm{H}})x(t) \\ x(t) = \frac{w(t)}{D} \in (0,1) \end{gathered} \tag{1}$$

where R_H and R_L denote the highest and lowest resistance state respectively. $w(t)$ is the time-independent length of the doped region. $x(t)$ is the internal state variable with the range of [0, 1] and its differential equation is given by

$$\frac{dx}{dt} = ki(t) f_{\mathrm{p}}(x),\ k = \frac{\mu_{\mathrm{v}} R_{\mathrm{L}}}{D^2} \tag{2}$$

where $i(t)$ is the current passing through the memristor, $f_p(x)$ is the so-called window function which is able to model the inevitable nonlinear ionic drift phenomenon near the boundaries of nanoscale devices [34], and parameter μ_v is the average ion mobility with the approximate value of 10^{-14} $m^2s^{-1}V^{-1}$.

In particular, when the window function is set as $f(x) = 4x\text{-}4x^2$ which is a special case of the *Joglekar* function with the subscript p=1, the memristor model is closer to the real memristive device and the relevant memristance can be rewritten as [35]

$$M(t) = R_{\mathrm{L}} + \Delta R \cdot \frac{1}{Ae^{4kq(t)} + 1} \tag{3}$$

where $A=(R_H-M_0)/(M_0-R_L)$ is a constant and M_0 is the initial memristance with t=0. ΔR denotes the difference of the two limit memristances, i.e., $\Delta R=R_H-R_L$.

After the differential operation, Eq. (1) leads to

$$\begin{aligned}\frac{dM(t)}{dt} &= -\Delta R\frac{dx(t)}{dt} \\ &= a(-M^2(t)+bM(t)+c)i(t)\end{aligned} \tag{4}$$

where the variables a=4k/-ΔR, b=R_L+R_H and c=-$R_\mathrm{L}R_\mathrm{H}$ are all constants.

Furthermore, by integrating both sides of Eq. (4) and assuming the initial condition q_0=0, the total quantity of electric charge required for memristance variation from the initial value M_0 to the objective value M_{Obj} can be calculated by

$$q(M_{Obj}) = \frac{1}{a\Delta R}\cdot\ln\left(\frac{(-M_{Obj}+R_\mathrm{L}+\varepsilon)(-M_0+R_\mathrm{H}+\varepsilon)}{(-M_{Obj}+R_\mathrm{H}+\varepsilon)(-M_0+R_\mathrm{L}+\varepsilon)}\right) \tag{5}$$

where the extra coefficient ε is an extremely small constant. It is utilized to make sure that Eq. (5) is valid in any case.

When the switching time required for memristance variation is a fixed time slice ΔT_q, the corresponding current I can be obtained by

$$I = q(M_{Obj}) / \Delta T_q \tag{6}$$

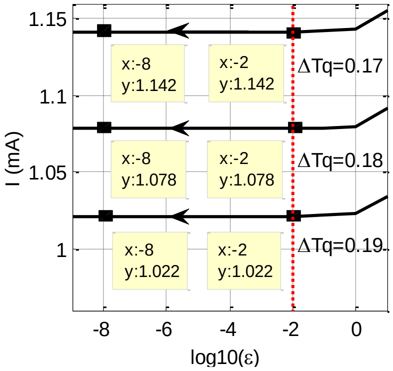

Fig. 2: The relationship between the $\log_{10}(\varepsilon)$ and the applied direct current under different switching time (ΔT_q =[0.17, 0.18, 0.19], Unit: Second), and the parameter setting is provided as below, R_L=100Ω, R_H=16kΩ, M_0=200Ω, M_{Obj}=15 kΩ and D=10nm.

Especially, when the coefficient ε is sufficiently small ($\varepsilon \leq 10^{-2}$), the switching time for memristance variation ΔT_q keeps a stable one-to-one correspondence with the amplitude of the current I, as shown in Fig. 2. Meanwhile, it is noted that the small time slice leads to a large current, which means when the ΔT_q is small enough, the input stimulus can be deemed as a current pulse with large amplitude.

3. Design of memristor-based pulse coupled neural network

In this section, the previously discussed HP memristor is applied to the classical PCNN model for the implementation of the variable linking coefficient. The specific description with relevant circuit analysis is provided as follows.

3.1 Classical PCNN model

According to the literature [1-3], PCNN is a kind of self-organizing feedback network with numerous integrate-and-fire neurons. And the basic structure of the PCNN neuron is actually a dynamic nonlinear system, as shown in Fig. 3.

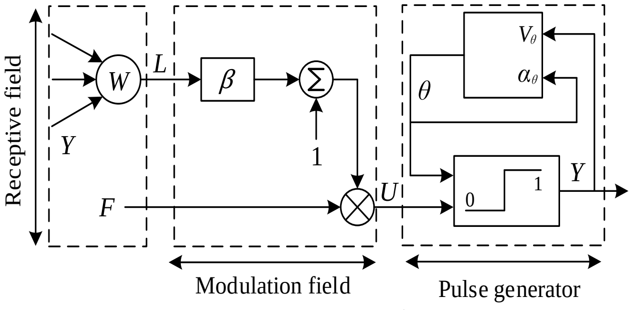

Fig. 3: The concrete composition of PCNN neuron

From Fig. 3, the neuron is composed of three subsections, where the leftmost dashed box is the receptive field, whose primary function is to receive input signals from the neighboring neurons and external stimulus, corresponding to linking inputs L and feeding inputs F respectively. The feeding inputs are multiplied with the biased and the multiplied linking inputs; to create the total internal activity item U which constructs the modulation field (the central part). Moreover, the remaining part, namely the pulse generator, is made up of a step function generator and a threshold signal generator. After the comparison between the internal activity item U and the dynamic threshold θ, the response of the neuron can be acquired. Specifically, when $U > \theta$, the neuron is in the firing state, the pulse generator is switched on and the relevant output Y is set to 1. Otherwise, when $U \leq \theta$, the neuron turns into the non-firing state, the pulse generator is switched off and the output Y is consequently reset to 0. The corresponding mathematical description is given by [3]

$$F_{ij}[n] = S_{ij} \tag{7a}$$

$$L_{ij}[n] = V_L \sum_{kl} w_{ijkl} Y_{kl}[n-1] \tag{7b}$$

$$U_{ij}[n] = F_{ij}[n]\left(1+\beta L_{ij}[n]\right) \tag{7c}$$

$$\theta_{ij}[n] = e^{-\alpha_\theta}\theta_{ij}[n-1] + V_\theta Y_{ij}[n-1] \tag{7d}$$

$$Y_{ij}[n] = step\left(U_{ij}[n]-\theta_{ij}[n]\right) = \begin{cases} 1, U_{ij}[n] > \theta_{ij}[n] \\ 0, U_{ij}[n] \le \theta_{ij}[n] \end{cases} \tag{7e}$$

where $F_{ij}[n]$ and $L_{ij}[n]$ are the feeding inputs and linking inputs of (i, j) neuron at the n^{th} iteration. $U_{ij}[n]$, $\theta_{ij}[n]$ and $Y_{ij}[n]$ are the internal activity item, dynamic threshold, and output of the neuron respectively. S_{ij} is the external stimulus, β represents the linking coefficient, w_{ijkl} is the constant synaptic weights, V_L and V_θ are the magnitude scaling terms, and α_θ is the attenuation time constant of the threshold $\theta_{ij}[n]$.

3.2 Combination of the memristor crossbar array and PCNN

In this section, a memristor-based circuit with the crossbar array configuration is utilized to constitute an adaptive memristive pulse coupled neural network (MPCNN) with the adjustable linking coefficient β (as shown in Fig. 4). And the relevant hardware implementation scheme is further provided in Fig. 5, it is beneficial to deal with the inherent parameter estimation issue occurred in traditional PCNN.

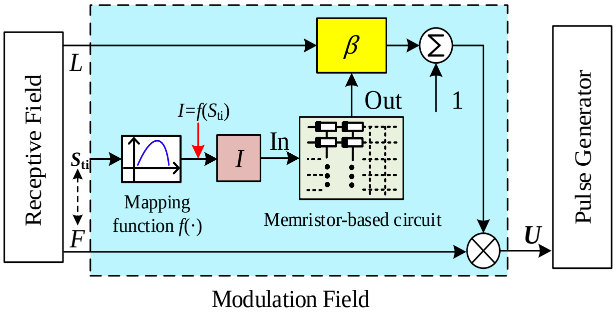

Fig. 4: The diagram of memristive PCNN (MPCNN) neuron

From Fig. 4, the modulation field is reconstituted by adding a concrete memristor-based circuit and a programmable current source. As the input of the memristive circuit, the variable current source I mainly depends on the input stimuli S_{ti} and the relevant mapping function f. Generally, the input stimuli is the relevant information related to the feeding inputs F, and the mapping function can be adjusted properly for different applications, which is conducive to achieve the optimal network performance. Consequently, the corresponding output of the memristor-based circuit can be obtained as the variable linking coefficient β in the MPCNN.

The specific implementation scheme of the adaptive linking coefficient β, based on the memristor crossbar array is designed and presented in Fig. 5(a). The fallow dashed box is the memristor crossbar array and the current-controlled memristor is formed at each crosspoint. The two pale blue boxes denote the necessary peripheral circuits and the specific implementations are demonstrated through two red ellipses in Fig. 5(b). Furthermore, the current sequence I_j (j=[1, n]) denotes the input of the circuit, which is determined by the input stimuli and the relevant mapping function. As a result, the linking coefficient β for each neuron can be obtained in the form of the output voltage, and the essential circuit analysis is illustrated as below.

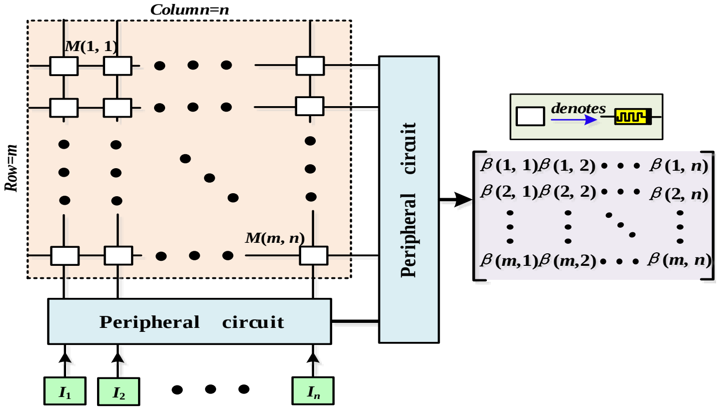

(a)

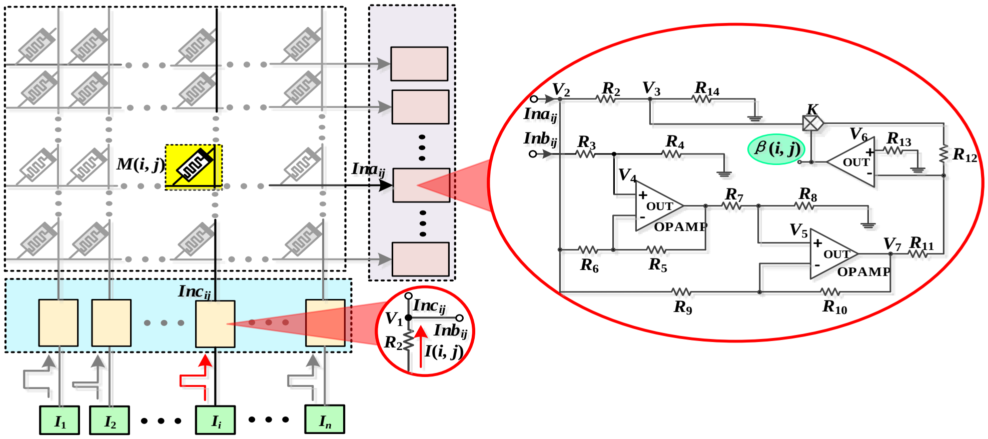

(b)

Fig. 5: The realization scheme of the adjustable linking coefficient β. (a) The specific hardware implementation block diagram. (b) The corresponding circuit composition.

For the sake of convenience, a general case is discussed in Fig. 5(b), where the Ina_{ij}, Inb_{ij} and Inc_{ij} are the corresponding I/O ports. Specifically, the $M(i, j)$ denotes the memristive device installed at the crosspoint (i, j), and $I(i, j)$ is the corresponding input current. According to the nodal voltage method, the circuit can be mathematically expressed as

$$I(i,j)=\frac{V_1(i,j)}{R_3+R_4}+\frac{V_1(i,j)-V_2(i,j)}{M(i,j)} \tag{8a}$$

$$\frac{V_2(i,j)-V_3(i,j)}{R_1}=\frac{V_1(i,j)-V_2(i,j)}{M(i,j)}+\left(\frac{R_4\cdot V_1(i,j)}{(R_3+R_4)R_6}-\frac{V_2(i,j)}{R_6}\right)+\left(\frac{R_8\cdot\left(V_1(i,j)-V_2(i,j)\right)}{(R_7+R_8)R_9}-\frac{V_2(i,j)}{R_9}\right) \tag{8b}$$

$$\frac{V_2(i,j)-V_3(i,j)}{R_1}=\frac{V_3(i,j)}{R_{14}} \tag{8c}$$

Assuming the R_n, n=[3, 10] are all identical resistors, the node voltage $V_1(i, j)$ can be computed by

$$V_1(i,j)=\frac{2R_3\left[(R_1+R_{14})\left(2M(i,j)+R_3\right)+M(i,j)R_3\right]}{(R_1+R_{14})\left(2M(i,j)+3R_3\right)+\left(M(i,j)+2R_3\right)R_3}\cdot I(i,j) \tag{9}$$

Moreover, R_3 is set at a much larger value than that of other circuit components in Eq. (9); all the node voltages $V_1(i, j)$, $V_2(i, j)$ and $V_3(i, j)$ can be further calculated by

$$\begin{cases} V_1(i,j)=\left(M(i,j)+R_1+R_{14}\right)\cdot I(i,j) \\ V_2(i,j)=\left(R_1+R_{14}\right)\cdot I(i,j) \\ V_3(i,j)=R_{14}\cdot I(i,j) \end{cases} \tag{10}$$

As the output of the entire circuit, the linking coefficient $\beta(i, j)$ can be given by

$$\beta(i,j)=\frac{R_{12}}{K\cdot R_{11}}\cdot\frac{V_1(i,j)-2V_2(i,j)+V_3(i,j)}{V_3(i,j)} \tag{11}$$

where constant K is the amplification factor. Substituting Eq. (10) into Eq. (11), we can get

$$\beta(i,j)=\frac{R_{12}}{K\cdot R_{11}}\cdot\frac{M(i,j)-R_1}{R_{14}} \tag{12}$$

Based on Eq. (3), if the value of R_1 is set to the lowest memristance (namely, $R_1=R_L$), Eq. (12) can be rewritten as

$$\beta(i,j)=\frac{\Delta R}{\kappa\left(1+Ae^{4kq(i,j)}\right)} \tag{13}$$

where $\kappa=KR_{11}R_{14}/R_{12}$ is a constant. Notably, when the initial memristance M_0 goes up to the largest value R_H, the constant A changes to zero and the linking coefficient β is a fixed value $\Delta R/\kappa$, irrespective of the electric charge variation.

According to the aforementioned description, two types of time-dependent currents are applied to the memristor $M(i, j)$ embedded within the presented circuit, and the corresponding linking coefficients can be illustrated in Fig. 6. The specific parameter setting is given as follows: $I_1(t)$={-0.5, -0.95, -1.8, -3.5, -6.8, -13.0, -94.0 Unit: mA} and the corresponding time interval is ΔT_j={1, 1/2, 1/4, 1/8, 1/16, 1/32, 1/256 Unit: Second}, j=[1, 8], $I_2(t)=(0.5t-1)/1000$ within the interval of t=[0, 4], R_L=100Ω, R_H=16kΩ, M_0=100Ω, D=10nm, $R_{3\sim10}$=2500kΩ, $R_2=R_{13}=R_{14}=R_{12}$=1Ω, K=1.

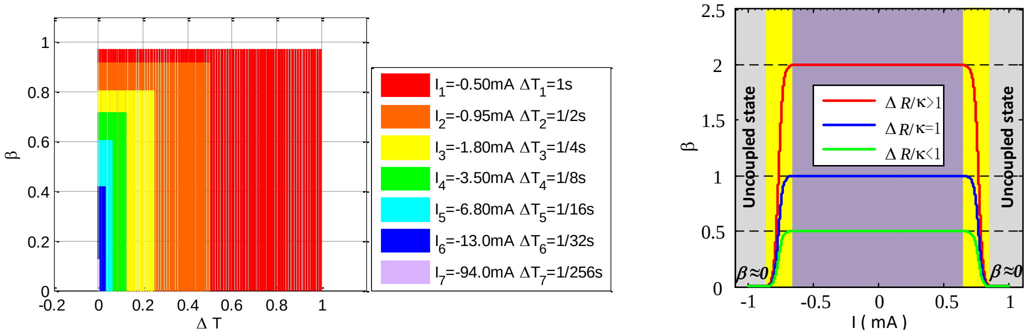

(a) (b)

Fig. 6: The input-output characteristics of the presented circuit. (a) The obtained linking coefficients under different direct currents. (b) The relationship between the linking coefficient β and the linear time-variant current I under the different κ, here R_{11}=[2ΔR, ΔR, 0.5ΔR].

In Fig. 6(a), the height of each colored histogram denotes the specific value of the linking coefficient under a given direct current. Especially, when the time interval is small enough (ΔT=1/256s), the direct current can be deemed as a current pulse and the linking coefficient can be obtained rapidly. Meanwhile, when a linear time-variant current is applied into the circuit, the linking coefficient β exhibits the unique threshold feature with the variation of the input current as shown in Fig. 6(b), and the ratio between the ΔR and the adjustment factor κ determines the upper boundary of the linking coefficient, i.e., $\beta_{max}=\Delta R/\kappa$. Specifically, when the linking coefficient changes to its minimum value, i.e., $\beta\approx 0$ (the gray region), the presented MPCNN is kept in an uncoupled state, which means the interconnected neurons are relatively isolated rather than regionally coupled with each other. As for any single neuron, it only receives the external stimulus S (in general S>0). When t=0, assuming the initial threshold $\theta(0)$=0, we can obtain $U(0)>\theta(0)$ based on Eq. (7c), which demonstrates the corresponding output $Y(0)$ is kept at the high level (firing state). According to Eq. (7d), the dynamic threshold $\theta(t)$ varies to V_θ (generally $V_\theta>S$) rapidly, and the output of the neuron returns to the low level. Notably, during the period that the dynamic threshold $\theta(t)$ exponentially decays to S, the output remains at a low level. Until $\theta(t)=S$, the output of the neuron will return to the high level. Hence, the relevant oscillating period T_1(S) can be calculated by

$$T_1(S)=\frac{1}{\alpha_\theta}\ln\left(\frac{V_\theta}{S}\right) \tag{14}$$

Similarly, when the linking coefficient β>0 (namely, the yellow and lavender regions), the interconnected neurons are regionally coupled with each other. Note that the red, blue, and green solid lines exhibited in the lavender region maintain the steady state, which indicates that the presented network is indeed a traditional PCNN with the fixed linking coefficient during this period. As for the yellow regions, where the linking coefficient changes with the electric charge variation, it essentially provides the possibility for the implementation of the adaptive neural network with the variable linking coefficient. For clarity and convenience, we further discuss the dynamic behaviors of the double-coupled neurons with the variable positive linking coefficient. Specifically, the external stimulus of the two neurons N_{ij} and N_{kl} are expressed as S_{ij} and S_{kl} (satisfying $S_{ij}>S_{kl}$) respectively. Without loss of generality, the initial thresholds of the two neurons are set to zero, i.e., $\theta_{ij}(0)=\theta_{kl}(0)=0$, which are smaller than the current internal activity items, and the two neurons are both in the firing state. The dynamic thresholds will increase to the given constant V_θ suddenly, and the corresponding internal activity items $U_{ij}= F_{ij}(1+ \beta L_{ij})$ and $U_{kl}= F_{kl}(1+ \beta L_{kl})$ will also grow due to the pulse stimulation generated from the two neurons themselves. Notably, because V_θ is larger than the internal activity items (U_{ij} and U_{kl}), when one of the two neurons fires for the first time, the output state of the other neuron will not be affected. Furthermore, based on $S_{ij}>S_{kl}$, the firing frequency of neuron N_{ij} is larger than that of neuron N_{kl}, namely, $f_{ij}>f_{kl}$. After the two neurons both release the pulses for the first time, the neuron N_{ij} will attain the firing state again at the time $t=T(S_{ij})$. Then the neuron N_{kl} receives the linking inputs generated from N_{ij} owing to the mutual coupling, and the relevant internal state changes from S_{kl} to $S_{kl}(1+ \beta L_{kl})$. At this moment, if $S_{kl}(1+ \beta L_{kl})> \theta_{kl}$, the neuron N_{kl} will be in the firing state as well. The entire process can be described by the fact that the neuron N_{kl} is captured by the neuron N_{ij}, and the synchronous firing state of the two neurons will be kept. On the contrary, if $S_{kl}(1+ \beta L_{kl})< \theta_{kl}$, the specific capture behavior will not happen, which means the two neurons (N_{ij} and N_{kl}) will generate the pulses with their respective frequencies.

Due to $L_{kl}=V_L$ (V_L is usually set to 1), and $\theta_{kl}= S_{ij}$, the range of the linking coefficient β for successful capture can be computed by

$$\beta>\frac{S_{ij}-S_{kl}}{S_{kl}} \tag{15}$$

Moreover, based on Eq. (13) and Eq. (15), the electric charge for successful capture satisfies

$$q<\frac{1}{4k}\ln\frac{S_{kl}\left(\Delta R+\kappa\right)-S_{ij}\kappa}{A\kappa\cdot\left(S_{ij}-S_{kl}\right)} \tag{16}$$

In addition, when the presented adaptive MPCNN is applied into the specific image processing, an appropriate mapping function between the input stimuli (usually the information of the input source image) and the input current I should be further built up. Particularly, different applications lead to different mapping functions, which is beneficial for guaranteeing that the presented neural network can always perform in an effective way. Meanwhile, the diversity of the mapping function makes the MPCNN a general adaptive model.

4. Multi-focus image fusion algorithm using MPCNN

As a major branch of digital image processing, image fusion is actually a process of integrating complementary information (mainly including the edge and texture information) from all the input images to generate a relatively high-resolution (HR) image which provides a more accurate description of the same scene than any of the individual images [12-16, 36-41]. In this section, the proposed MPCNN is further applied to the multi-focus image fusion with a more compact network topology. Based on the image orientation information measure, an appropriate mapping function is employed to achieve the input current *I*. After that, the corresponding fusion algorithm is presented, and the specific process description is given below.

4.1 Network topology of the multi-channel MPCNN

Based on the structural composition of the presented MPCNN, the number of channels can be changed to take the good scalability and portability into account. The single-channel model means that there exists only one external input channel for each neuron, which is indeed a structural defect for multi-focus image fusion. In other words, a single MPCNN with only one external input channel cannot realize the image fusion successfully. A group of MPCNNs (at least two MPCNNs) are required to complete the fusion task in general, which makes the fusion strategy inefficient and time-consuming. Hence, in order to tailor the best network performance for the image fusion, an improved model with multiple external input channels is exhibited in Fig. 7, where the number of channels is purposely adjusted and the multiple inputs can be received simultaneously.

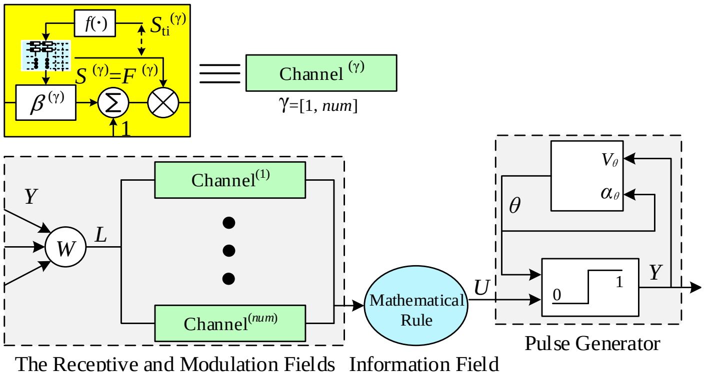

Fig. 7: The topology construction of the multi-channel MPCNN neuron

In Fig. 7, the multi-channel MPCNN model is a compact integration composed by the receptive and modulation fields, information field and the pulse generator, where the superscript γ within the range [1, *num*] represents the γth channel. Compared with the single-channel MPCNN, the additional external input channels and the information field (the pale blue ellipse) provide desirable convenience and efficiency improvement for the implementation of the information fusion. Note that the information field is responsible for selecting the maximum internal activity item in all symmetrical channels, and the specific mathematical rule is given by

$$U_{ij}\left[n\right]=\max\left(F_{ij}^{(1)}\left[n\right]\left(1+\beta^{(1)}L_{ij}\left[n\right]\right),\ldots,F_{ij}^{(num)}\left[n\right]\left(1+\beta^{(num)}L_{ij}\left[n\right]\right)\right) \tag{17}$$

$$F_{ij}^{(\gamma)}\left[n\right]=S_{ij}^{(\gamma)},\gamma=\left[1,2,\ldots num\right] \tag{18}$$

It is important to note that the mathematical description of other variables (including $L_{ij}[n]$, $\theta_{ij}[n]$ and $Y_{ij}[n]$) is consistent with the relevant parts expressed in Eq. (7). Particularly, we can conclude that the original single-channel MPCNN is a special case of the improved multi-channel MPCNN with the number of channels *num*=1.

4.2 Appropriate mapping function for multi-focus image fusion

In image fusion, the linking coefficient β generally determines how much important information of the input source images can be fused into the output image. In this subsection, an appropriate mapping function is designed to achieve the specific input currents flowing through all the crosspoints in the memristive circuit, and then the corresponding outputs, i.e., the linking coefficients, can be obtained within a controllable time. The concrete illustration is given below.

According to the existing physiological and psychological research [42, 43], the human visual system (HVS) is highly sensitive to the image edge orientation information. The image orientation information measure proposed in [42] provides an effective way to present the edges and texture features of the image, which is suitable for the construction of the mapping function in image fusion. Specifically, for a given image *P*, *P*(*i*, *j*) represents the pixel value at the point (*i*, *j*). The neighborhood $R_r(i, j)=\{(m, n)|\ i\text{-}r \le m \le i+r,\ j\text{-}r \le n \le j+r\}$ centred at the point (*i*, *j*) is divided into a shadow region (*AL*) and a blank region (*AR*) by a straight line $l\chi$ crossing through the central point as shown in Fig. 8. Parameter *r* denotes the radius of the neighborhood, and χ is the angle between $l\chi$ and the horizontal line. The image orientation information is defined by [42]

$$O\left(P(i,j)\right)=d_{\chi_{\max}}-d_{\chi_{\min}} \tag{19}$$

where

$$d_{\chi_{\max}}=\max_{0^\circ\le\chi\le180^\circ}\left(d_\chi\right) \tag{20a}$$

$$d_{\chi_{\min}}=\min_{0^\circ\le\chi\le180^\circ}\left(d_\chi\right) \tag{20b}$$

$$d_\chi=\left|f_{AL}-f_{AR}\right| \tag{20c}$$

$$f_{AL}=\sum_{(i,j)\in AL}I_m\left(i,j\right) \tag{20d}$$

$$f_{AR}=\sum_{(i,j)\in AR}I_m\left(i,j\right) \tag{20e}$$

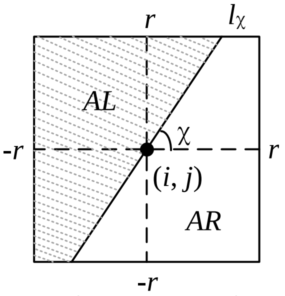

Fig. 8: The diagram of the orientation information measure

For simplicity, the mapping function between the input stimuli (i.e., the image orientation information) and the input current is briefly defined as

$$I\left(i,j\right)=f\left(S_{\text{ti}}\left(i,j\right)\right)=\xi O\left(P\left(i,j\right)\right) \tag{21}$$

where parameter ξ is a negative constant.

Especially, if the time interval ΔT_P is set to a sufficiently small value, the input current at the crosspoint (i, j) can be regarded as a large amplitude pulsed current. The adaptive linking coefficient related to the image orientation information can be effectively obtained by the memristor-based circuit, and its corresponding mathematical expression can be given by

$$\beta\left(i,j\right)=\frac{\Delta R}{\kappa\left(1+Ae^{4k\xi O\left(P\left(i,j\right)\right)\Delta T_P}\right)} \tag{22}$$

where $\xi O(P(i, j)) \cdot\Delta T_P$ is the electric charge variation $\Delta q(i, j)$.

According to Eq. (22), when the parameters ξ, ΔR, κ and A are given in advance, the large orientation information results in a large linking coefficient β, which means the source image with abundant edge and texture information will take a relatively high proportion in the fused image. This is consistent with the fact that the real neurons should have the different linking coefficients, and therefore of practical significance. Meanwhile, due to the unique parallel processing capability of the crossbar array configuration, the time required for obtaining the linking coefficient is approximately equal to ΔT_P, in spite of the network scale.

Notably, based on the specific fusion requirement, the linear mapping function $f(\cdot)$ written in Eq. (21) can be further defined as a nonlinear one with more complex expression. The image orientation information measure is not the only option for the input stimuli, other available information related to the input source image (like contrast saliency, structure saliency, geometric moment, sharpness, etc.) can also be utilized for the construction of the mapping function in image fusion. Both of these make the entire design process more flexible and reasonable.

4.3 Description of the multi-focus image fusion algorithm

Based on the preliminary work, the specific realization process of the multi-focus image fusion is demonstrated in Fig. 9. Notably, the input source images P^γ (γ=[1, 2]) should be registered with the same size and resolution, and the corresponding output is the reconstructed fused image F_u. In essence, the entire input-output process is described as follows.

Step 1: Initialization. The first step is mainly for the parameter setting, including the global network parameters and the device parameters in the memristive circuit.

Step 2: Acquisition of the variable linking coefficient. When the two spatially registered multi-focus images are given, the relevant orientation information $O(P^\gamma)$ can be computed based on Eqs. (19) - (20). The input current I^γ of the memristor-based circuit can be derived from Eq. (21), and the corresponding output of the circuit, i.e., the linking coefficient β^γ, can be obtained within a small-time interval.

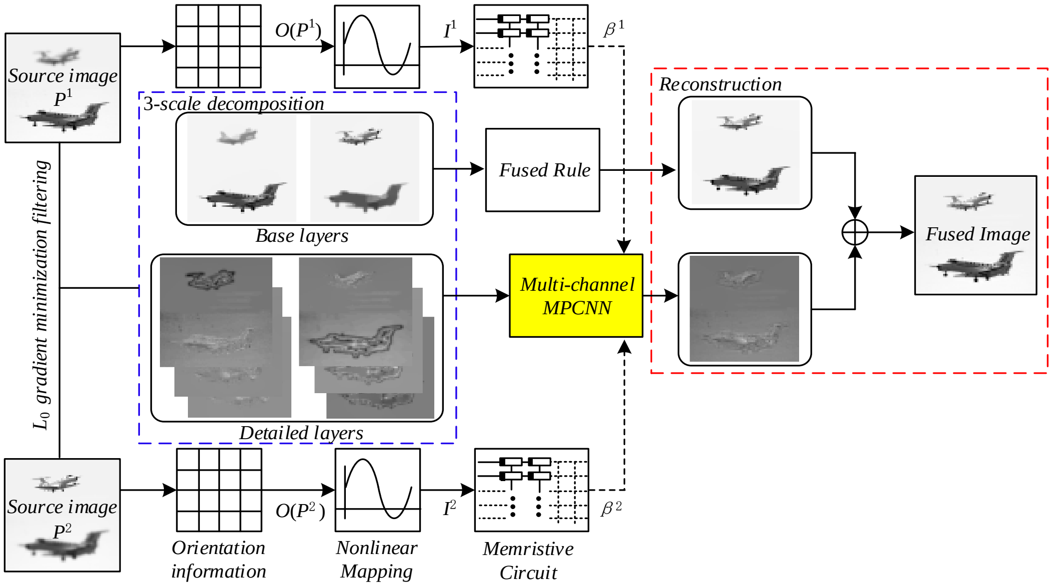

Fig. 9: The implementation block diagram of the multi-focus image fusion algorithm

Step 3: Decomposition. Specifically, the source images are decomposed into two parts after *N*-scale L_0 gradient minimization smoothing filtering [44], where the base layer contains the large-scale variations in intensity, and the detail layers contain the main detail information (edge information, texture details, etc.) of the source image. Their specific expressions can be obtained respectively by

$$Base_l^\gamma = GMSF\left(Base_{l-1}^\gamma, \lambda_l^\gamma\right) \tag{23a}$$

$$Detail_l^\gamma = Base_{l-1}^\gamma - Base_l^\gamma, \, l = [1, N] \tag{23b}$$

where $Base_l^\gamma$ and $Detail_l^\gamma$ are the base and detail image in the l^{th} layer respectively, *GMSF* is the so-called L_0 gradient minimization smoothing filtering with the regularized parameter λ_l^γ . Here, the initial base image $Base_0^\gamma$ is set as the input image P^γ, and the regularized parameter is set to $\lambda_l^\gamma = 0.02$. Notably, the original image P^γ can be indistinguishably reconstructed by synthesizing the N^{th} base image and all the detail images.

Step 4: Fusion of the base images. Due to the fact that the Sum-Modified-Laplacian (SML) proposed in [45] is able to measure variation of pixels, the fusion rule of the N^{th} level base layers can be described as below,

$$\begin{aligned} ML_N^\gamma(i, j) = {} & \left|2Base_N^\gamma(i, j) - Base_N^\gamma(i-1, j) - Base_N^\gamma(i+1, j)\right| \\ & + \left|2Base_N^\gamma(i, j) - Base_N^\gamma(i, j-1) - Base_N^\gamma(i, j+1)\right| \end{aligned} \tag{24}$$

$$SML_N^\gamma(i, j) = \sum_{w_r=-Row}^{Row} \sum_{w_c=-Col}^{Col} W(w_r, w_c)\left[ML_N^\gamma(i + w_r, j + w_c)\right]^2 \tag{25}$$

where $ML_N^\gamma(i, j)$ denotes the modified Laplacian at the location (*i*, *j*), $W(w_r, w_c)$ is a measure window with the size of $(2Row+1)\times(2Col+1)$. In the subsequent experiments, *Row*=*Col*=2 and the measure window is set to

$$W(w_r, w_c) = \frac{1}{81}\begin{bmatrix} 1 & 2 & 3 & 2 & 1 \\ 2 & 4 & 6 & 4 & 2 \\ 3 & 6 & 9 & 6 & 3 \\ 2 & 4 & 6 & 4 & 2 \\ 1 & 2 & 3 & 2 & 1 \end{bmatrix} \tag{26}$$

which satisfies the normalization rule $\sum_{w_r}\sum_{w_c} W(w_r, w_c) = 1$.

As a result, the fused base image F_b can be obtained by

$$F_b(i, j) = \begin{cases} Base_N^1(i, j) & if \; SML_N^1(i, j) \ge SML_N^2(i, j) \\ Base_N^2(i, j) & otherwise \end{cases} \tag{27}$$

This means that the pixels with larger *SML* are chosen as the target pixels of the fused base image.

Step 5: Fusion of the detail images. Since the PCNN is capable of catching and detecting the image salient information effectively, it is suitable for the implementation of the detail images fusion. The relevant fusion rule can be described as below.

1) All the detail images are transmitted into the MPCNN via their respective channels.
2) Based on the initial operation expressed in **Step 1** and the variable linking coefficient obtained in **Step 2**, the variables $L_{ij}[n]$, $U_{ij}[n]$, $\theta_{ij}[n]$, and $Y_{ij}[n]$ in the n^{th} iteration can be computed according to Eqs. (7), (17), and (18).
3) If n=N_s is satisfied, the iteration operation stops, and the fused detail image F_{dl} for each level can be obtained as follows

$$F_{dl}(i,j)=\begin{cases} Detail_l^1(i,j) \ if U_{ij,l}(N_s)=U_{ij,l}^1(N_s) \\ Detail_l^2(i,j) \ if U_{ij,l}(N_s)=U_{ij,l}^2(N_s) \end{cases} \tag{28}$$

Note that the total iteration number N_s can be determined by the so-called time matrix [16], and all the interconnected neurons are permitted for firing only once during the whole fusion process.

Step 6: Image reconstruction. The fused image F_u is obtained by integrating the fused base image F_b and the fused detail images F_{dl}.

$$F_u = F_b + \sum_{l=1}^{N} F_{dl} \tag{29}$$

Actually, the **Step 1** and **Step 2** are responsible for the parameter setting of the presented MPCNN, with the remaining steps (i.e., **Steps 3-6**) are for the specific description of the multi-focus image fusion.

5. Computer simulations and analysis

In order to demonstrate the effectiveness of the presented fusion strategy, a series of contrast experiments with relevant analysis (including subjective and objective analysis) are conducted based on the MATLAB software platform (operation environment: CPU Core i7-4710HQ, memory 16GB). The specific parameter setting for the multi-channel MPCNN and the memristive circuit is provided in Table 1.

Table 1: The collection of the network parameters and device parameters

Multi-channel MPCNN		**Memristor-based circuit**	
Variable	**Value**	**Variable**	**Value**
V_L	1	R_1	100Ω
V_θ	30	R_2	1Ω
α_θ	0.25	R_i,[i=3,10]	2500kΩ
w	$\begin{bmatrix} 0.707 & 1 & 0.707 \\ 1 & 0 & 1 \\ 0.707 & 1 & 0.707 \end{bmatrix}$	R_{12}	1Ω
		R_{14}	1Ω
		R_{11}	19.9kΩ
num	2	R_L	100Ω
N_S	200	R_H	20kΩ
ξ	-0.25	R_0	100.1Ω
ΔT_P	25μs	K	1

From Table 1, the multi-channel MPCNN with the initial conditions $\theta_{ij}(0)$=0, $L_{ij}(0)$=0, $Y_{ij}(0)$=0, and $U_{ij}(0)$=0 is built up. Based on the two registered multi-focus bottle images in Fig. 10(a), the whole acquisition process of the variable linking coefficient is demonstrated step-by-step. Specifically, Fig. 10(b) denotes the corresponding orientation information of the two source images from Eq. (19) and Eq. (20), where the regions containing rich edge and texture information mean the corresponding orientation information is relatively large. For simplicity, two red rectangles (i.e., Area1 and Area2) with the size of 32x32 are labeled randomly, which provides a general example to illustrate how to obtain the linking coefficients effectively. According to the labeled regions (the enlarged versions can be seen in Fig. 10(c)) and the linear mapping function in Eq. (21), the input currents of the memristor-based circuits can be acquired as exhibited in Fig. 10(d), where the height of the color bar denotes the specific amplitude of single current pulse for each neuron. Similarly, the corresponding outputs (i.e., the adaptive linking coefficient) of the memristor-based circuit are demonstrated in the Fig. 10(e) with the same 3D-histogram representation, and the higher bar indicates the obtained linking coefficient is relatively large.

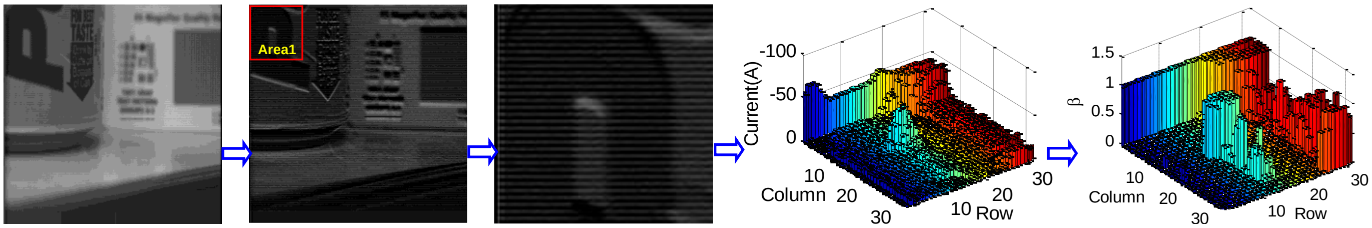

(a1) (b1) (c1) (d1) (e1)

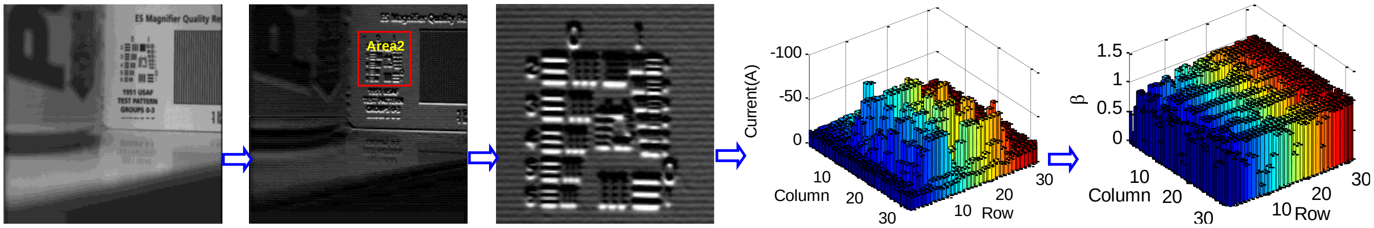

(a2) (b2) (c2) (d2) (e2)

Fig. 10. The acquisition process of the variable linking coefficient. (a1) ~ (a2) The multi-focus source images (Size: 128x128). (b1) ~ (b2) The orientation information of the multi-focus bottle images respectively. (c1) ~ (c2) The enlarged Area1 and Area 2 (Size: 32x32). (d1) ~ (d2) The corresponding input currents of the memristor-based circuits for the labeled Area1 and Area 2. (e1) ~ (e2) The available linking coefficients for the two labeled rectangles.

After the 3-scale L_0 gradient minimization smoothing filtering, the two source images are decomposed into twelve components (as exhibited in Fig. 11), including three base images and three detail images for each source image. Then, in order to extract and preserve more image edge and texture information, the generated base images and detail images are fused by using different fusion rules as demonstrated in the algorithm description. Concretely, the SML is served as a criterion to fuse the base images, and the MPCNN is applied in the fusion of all the detail images. The final fused image can be reconstructed by synthesizing the fused base image and detail images effectively.

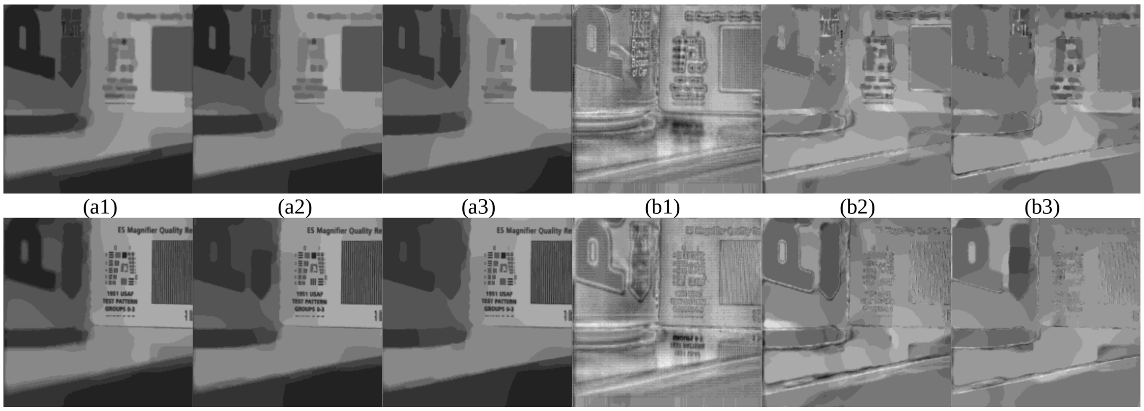

(a1) (a2) (a3) (b1) (b2) (b3)

(c1) (c2) (c3) (d1) (d2) (d3)

Fig. 11. The 3-scale image decomposition by L_0 gradient minimization smoothing filtering. (a1) ~ (a3) The base images for the left-focus source image. (b1) ~ (b3) The detail images for the left-focus source image. (c1) ~ (c3) The base images for the right-focus source image. (d1) ~ (d3) The detail images for the right-focus source image.

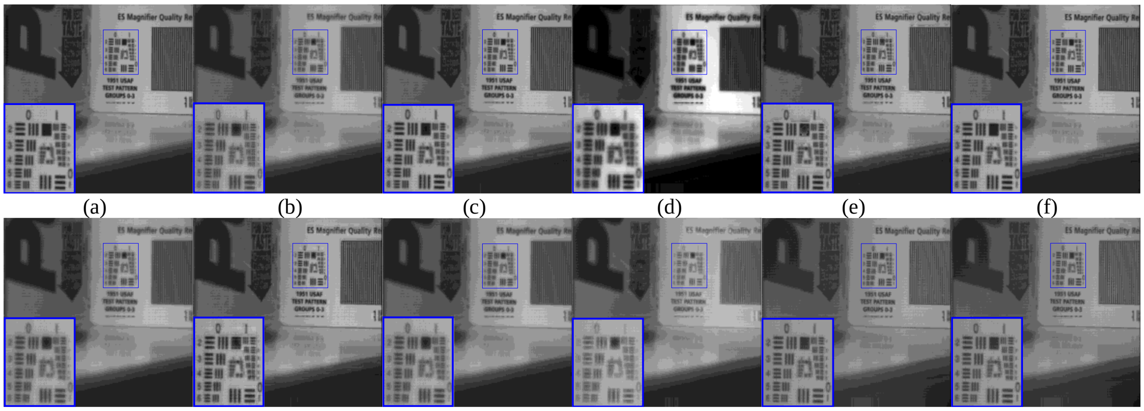

(a) (b) (c) (d) (e) (f)

(g) (h) (i) (j) (k) (l)

Fig. 12. The fused bottle images under different algorithms. (a) Proposed algorithm. (b) Classical PCNN algorithm [12]. (c) Improved PCNN algorithm [13]. (d) m-PCNN algorithm [14]. (e) Wavelet-based Contourlet Transform (WBCT)+PCNN algorithm [15]. (f) Non-sampled Contour Transform (NSCT)+PCNN algorithm [16]. (g) Principal Component Analysis (PCA) algorithm [36]. (h) Discrete Wavelet Transform (DWT) algorithm [37]. (i) Averaging algorithm [38]. (j) Ratio pyramid algorithm [39]. (k) Filter-Subtract-Decimate (FSD) pyramid algorithm [40]. (l) Gradient pyramid algorithm [41].

During the contrast experiment, the fused images generated by twelve different fusion algorithms are exhibited in Fig. 12, where the regions labeled by the blue rectangles can be used for the subjective analysis. It is clear that all these fused images contain some salient features extracted from the both two source images. However, the visual impact of the images shown in Figs. 12(b), 12(d), 12(g), 12(i) ~ 12(l) is not as good as that of images based on other fusion algorithms on account of the image ghosting artifact and edge interruption issues. In other words, the remaining fused images in Figs. 12(a), 12(c), 12(e)~12(f) and 12(h) possess relatively sharp edges and fine details.

Table 2: The image quality assessment indexes for fusion performance evaluation [46, 47]

Assessment index	Concrete meaning	Mathematical expression
Mutual information	Defining as the sum of mutual information between the source image and the fused image.	$MI = \sum_{g,f} p_{GF}(g,f)\log\frac{p_{GF}(g,f)}{p_G(g)\,p_F(f)} + \sum_{h,f} p_{HF}(h,f)\log\frac{p_{HF}(h,f)}{p_H(h)\,p_F(f)}$
Mean structural similarity	Representing the similar degree between the source images and the final fused image.	$SSIM(G,F_u)=\left(\frac{2\mu_g\mu_f+c_1}{\mu_g^2+\mu_f^2+c_1}\right)\cdot\left(\frac{2\sigma_g\sigma_f+c_2}{\sigma_g^2+\sigma_f^2+c_2}\right)\cdot\left(\frac{\mathrm{cov}_{gf}+c_3}{\sigma_g\sigma_f+c_3}\right)$ $MSSIM(G,H,F_u)=\left(SSIM(G,F_u)+SSIM(H,F_u)\right)/2$
Spatial frequency	Indicating the overall activity in the fused image.	$SF=\sqrt{RF^2+CF^2}$
Information entropy	Denoting the specific information content of the final fused image.	$IE=-\sum_{i=0}^{L_e-1} p_i \log_2(p_i)$
$Q^{GH/Fu}$	Considering the amount of edge information transferred from the source images to the fused image	$Q^{GH/F_u}=\frac{\sum_{n_r=1}^{N_R}\sum_{n_c=1}^{N_C}\left(Q^{GF}(n_r,n_c)w^G(n_r,n_c)+Q^{HF}(n_r,n_c)w^H(n_r,n_c)\right)}{\sum_{i=1}^{N_R}\sum_{j=1}^{N_C}\left(w^G(i,j)+w^H(i,j)\right)}$

Note: G and H are the two source images, F_u is the fused image. p_{GF} and p_{GF} are the joint histograms of the source images and the fused image. p_G, p_H and p_F are the corresponding histograms of G, H and F_u. μ_g and μ_f are the average value of G and F_u. σ_g (σ_f) and cov_{gf} are the relevant standard deviation and covariance of G and F_u. c_1, c_2 and c_3 are all constants. RF and CF are the row frequency and column frequency of the fused image respectively. L_e is the overall gray level and p_i is the occurrence probability of pixel i. N_R x N_C is the size of the image, Q^{GF} (Q^{HF}) means the relative strength between the source image and fused image, and w^G (w^H) is the edge strength function which reflects the importance of Q^{GF} (Q^{HF}).

Notably, the subjective visual analysis for image fusion mainly depends on the human visual system (HVS) which refers to several factors, such as image category, observers' preference, mission requirement, and so forth. Especially, for the cases when the visual difference is small (as shown in Figs. 12(a), 12(c), 12(e) ~ 12(f) and 12(h)), it is difficult to provide the precise analysis and sensible judgment for the final fusion effect. Hence, a series of objective image quality assessment indexes are introduced in Table 2, and the specific objective analysis for the final fused images is described as below.

Table 3: The objective performance evaluation of the fused images under different fusion algorithms

	MI	*MSSIM*	*SF*	*IE*	$Q^{GH/Fu}$
Proposed method	**5.9825**	**0.9089**	**23.1608**	**7.1402**	**0.7077**
Classical PCNN	5.2313	0.9071	21.8151	7.1216	0.6567
Improved PCNN	5.1426	0.9034	23.0320	7.1237	0.6774
m-PCNN	4.0998	0.7479	20.4400	7.1269	0.4505
WBCT+PCNN	5.7831	0.8847	23.0103	7.1192	0.6602
NSCT+PCNN	5.1098	0.9028	23.1093	7.1328	0.6842
PCA	4.7985	0.9217	20.6202	7.0872	0.6316
DWT	4.3618	0.8896	23.1562	7.1423	0.6682
Averaging method	4.7459	0.9215	20.5814	7.0865	0.6445
Ratio pyramid	4.6211	0.9066	20.9133	7.1205	0.6398
FSD pyramid	4.2631	0.9005	21.0699	6.9577	0.6233
Gradient pyramid	4.2874	0.9031	21.0038	6.9731	0.6229

Based on Table 3, the algorithm presented in this paper has the largest mutual information (*MI*=5.9825) among the twelve fusion algorithms, which means the fused image created by the proposed method acquires the most information from the two source images. The presented method does not have the outstanding advantage in terms of mean structural similarity (only lies in the third place *MSSIM*=0.9089), which illustrates that the presented method is inferior to the PCA and averaging method in the aspect of maintaining the image luminance, image contrast ratio and image structure. Meanwhile, the specific data shows that the presented method keeps its leading position in spatial frequency (*SF*). However, compared with the improved PCNN, WBCT+PCNN, NSCT+PCNN, and DWT method, the competitive superiority is not evident. Furthermore, except for DWT method, the fused image generated by the presented method has the largest information entropy (*IE*=7.1402) among the remaining fusion algorithms, which means less information is lost during the entire fusion process. In addition, based on the edge-preserving decomposition strategy and the adjustable linking coefficient β, the presented method possesses the largest $Q^{GH/Fu}$, which denotes that more texture and edge information is effectively saved into the fused image.

6. Conclusions

In this paper, a more practical TiO_2/TiO_{2-x} memristor model with its salient features is initially investigated. According to the specific theoretical description and formula derivation, the one-to-one correspondence between the switching time for memristance variation and the input current can be acquired. Next, taken account of the inherent parameter estimation issues occurred in the traditional PCNN model, a novel circuit composed of the memristor crossbar array and the relevant peripheral circuits is designed in detail, which is able to simulate the adaptive linking coefficient β varying with the different input signals. Particularly, due to the advantages of large-scale parallel processing, the crossbar array construction provides the benefits of high-efficiency and time-saving. Meanwhile, the mapping function, as an important component affecting the value of the linking coefficient β, should be designed appropriately for the final applications, which makes the presented MPCNN a more general network model. For the purpose of verification, the presented MPCNN is further applied into the multi-focus image fusion task with a compact network topological structure (multi-channel configuration). An appropriate mapping function representing the direct relationship between the input current of the memristive circuit and the input stimuli (the image orientation information) is constructed, following by the specific illustration of an improved multi-focus image fusion algorithm. Finally, the experimental results demonstrate the high-performance of the presented algorithm in terms of the visual effect and the objective evaluation criteria (including MI, $MSSIM$, SF, IE, $Q^{GH/Fu}$).

Acknowledgments

This work was supported by National Natural Science Foundation of China [Grant Nos. 61571394, 61503341].

References

[1] R. Eckhorn, et al., Feature linking via synchronization among distributed assemblies: Simulations of results from cat visual cortex, *Neural Comput.* 2 (3) (1990) 293–307.

[2] J. L. Johnson, M. L. Padgett, PCNN models and applications, *IEEE Trans. Neural Netw.* 10 (3) (1999) 480–498.

[3] Z. Wang, Y, Ma, F. Cheng, et al., Review of pulse-coupled neural networks. *Image. Vision Comput.* 28 (1) (2010) 5–13.

[4] Y, Ma, D. Lin, B. Zhang, et al., A novel algorithm of image enhancement based on pulse coupled neural network time matrix and rough set, *Fuzzy Systems and Knowledge Discovery (FSKD). 4th International Conference on. IEEE.* 3 (2007) 86–90.

[5] K. Zhan, J. Teng, J. Shi, Q. Li, M. Wang, Feature-linking model for image enhancement. *Neural Comput* 28(6) (2016) 1072–1100.

[6] M. Li, W. Cai, X. Li, An adaptive image segmentation method based on a modified pulse coupled neural network. *International Conference on Natural Computation* (2006) 471-474.

[7] C. Gao, D. Zhou, Y. Guo, Automatic iterative algorithm for image segmentation using a modified pulse-coupled neural network. *Neurocomputing*, 119 (2013) 332-338.

[8] C. Shen, D. Wang, S. Tang, et al., Hybrid image noise reduction algorithm based on genetic ant colony and PCNN. *Visual Comput.*, 33(11) (2017) 1373-1384.

[9] X. Deng, Y. Ma, M. Dong, A new adaptive filtering method for removing salt and pepper noise based on multilayered PCNN. Pattern *Recogn. Lett.*, 79 (2016) 8-17.

[10] R. P. Broussard, S. K. Rogers, M. E. Oxley, et al., Physiologically motivated image fusion for object detection using a pulse coupled neural network, *IEEE Trans. Neural Netw.* 10 (3) (1999) 554–563.

[11] Z. Yang, M. Dong, Y. Guo, et al., A new method of micro-calcifications detection in digitized mammograms based on improved simplified PCNN. *Neurocomputing*, 218 (2016) 79-90.

[12] Z. Wang, Y. Ma, J. Gu, Multi-focus image fusion using PCNN. *Pattern Recogn.* 43 (6) (2010) 2003–2016.

[13] S. Zhu, L. Wang, S. Duan, Memristive pulse coupled neural network with applications in medical image processing. *Neurocomputing* 227 (2017) 149–157.

[14] Z. Wang, Y. Ma, Medical image fusion using m-PCNN. *Inform. Fusion* 9 (2) (2008) 176–185.

[15] X. Wang, L. Chen, Image fusion algorithm based on spatial frequency-motivated pulse coupled neural networks in wavelet based contourlet transform domain, *IEEE International Conference on Environmental Science and Information Application Technology (ESIAT)* 2 (2010) 411–414.

[16] T. Xiang, L. Yan, R. Gao, A fusion algorithm for infrared and visible images based on adaptive dual-channel unit-linking PCNN in NSCT domain. *Infrared Physics Techn.*, 69 (2015) 53-61.

[17] L. Chua, Memristor—the missing circuit element, *IEEE Trans. Circuit Theory* 18 (5) (1971) 507–519.

[18] D. B. Strukov, G. S. Snider, D. R. Stewart, and R. S. Williams, The missing memristor found, *Nature* 453 (7191) (2008) 80–83

[19] S. Shin, K. Kim, S. M. Kang, Resistive computing: Memristors-enabled signal multiplication. *IEEE Trans. Circuits Syst. I, Reg.* Papers 60 (5) (2013) 1241–1249.

[20] I. Gupta, A. Serb, A. Khiat, et al., Improving detection accuracy of memristor-based bio-signal sensing platform. *IEEE Trans. Biomed. Circuits Syst.*, 11 (1) (2017) 203-211.

[21] X. Hu, G. Feng, S. Duan, et al. Multilayer RTD-memristor-based cellular neural networks for color image processing. *Neurocomputing*, 162 (2015) 150-162.

[22] S. Duan, X. Hu, et al., Memristor-based cellular nonlinear/neural network: design, analysis, and applications. *IEEE Trans. Neural Netw. Learn. Syst.* 26 (6) 2015 1202–1213.

[23] A. Chandrasekar, R. Rakkiyappan, Impulsive controller design for exponential synchronization of delayed stochastic memristor-based recurrent neural networks. *Neurocomputing*, 173 (2016) 1348-1355.

[24] H. Bao, J. H. Park, J. Cao, Exponential synchronization of coupled stochastic memristor-based neural networks with time-varying probabilistic delay coupling and impulsive delay. *IEEE Trans. Neural Netw. Learn. Syst.* 27 (1) (2016) 190-201.

[25] S. Duan, Z. K. Dong, et al., Small-world Hopfield neural networks with weight salience priority and memristor synapses for digit recognition, *Neural Comput. Appl.* (2015) 1–8.

[26] Y. Zhang, Y. Li, X. Wang, et al., Synaptic characteristics of Ag/AgInSbTe/Ta-based memristor for pattern recognition applications. *IEEE Trans Electron Devices*, 64 (4) (2017) 1806-1811.

[27] P. Zhang, C. Li, T. Huang, et al., Forgetting memristor based neuromorphic system for pattern training and recognition. *Neurocomputing*, 222 (2017) 47-53.

[28] A. Ascoli, R. Tetzlaff, L. Chua, et al., History erase effect in a non-volatile memristor, *IEEE Trans. Circuits Syst. I, Reg.* Papers. 63 (3) (2016) 389–400.

[29] A. Ascoli, R. Tetzlaff, L. Chua, The first ever real bistable memristors—part II: design and analysis of a local fading memory system. *IEEE Trans Circuits Syst. II: Exp. Briefs*, 63 (12) (2016) 1096-1100.

[30] S. Hamdioui, M. Taouil, Z. Haron, Testing open defects in memristor-based memories. *IEEE Trans Comput.*, 2015, 64(1): 247-259.

[31] P. M. Sheridan, F. Cai, C. Du, et al., Sparse coding with memristor networks. *Nat. Nanotechnol*. 2017.

[32] S. N. Truong, K. Van Pham, W. Yang, et al., Time-shared twin memristor crossbar reducing the number of arrays by half for pattern recognition, *Nanoscale Res. Lett.*. 12 (1) (2017) 205–210.

[33] G. C. Adam, B. D. Hoskins, M. Prezioso, et al., 3-D memristor crossbars for analog and neuromorphic computing applications. *IEEE Trans. Electron Devices*, 64 (1) (2017) 312-318.

[34] Z. Biolek, D. Biolek, and V. Biolkova, Spice model of memristor with nonlinear dopant drift, *Radioengineering*. 18 (2) (2009).

[35] Z. Dong, C. Li, D. Qi, et al., Multiple memristor circuits parametric fault diagnosis using feedback-control doublet generator, *IEEE Access*. 4 (2016) 2604–2614.

[36] V. P. S. Naidu, J. R. Raol, Pixel-level image fusion using wavelets and principal component analysis, *Defence Sci. J.* 58 (3) (2008) 338–352.

[37] G. Pajares, J. M. De La Cruz, A wavelet-based image fusion tutorial, *Pattern Recogn.* 37 (9) (2004) 1855-1872.

[38] G. Piella, H. Heijmans, A new quality metric for image fusion, *IEEE International Conference on Image Processing (ICIP)* 3 (2003) 173–176.

[39] A. Toet, Image fusion by a ratio of low-pass pyramid, *Pattern Recogn. Lett.* 9 (4) (1989) 245–253.

[40] H. Anderson, A filter-subtract-decimate hierarchical pyramid signal analyzing and synthesizing technique. *US Patent* 4 718 (104) (1988) 1–5.

[41] V. S. Petrovic, C. S. Xydeas, Gradient-based multi-resolution image fusion, *IEEE Trans. Image process.* 13 (2) (2004) 228–237.

[42] J. Li, W. Y. Yau, H. Wang, Combining singular points and orientation image information for fingerprint classification, *Pattern Recogn*. 41 (1) (2008) 353–366.

[43] W. Lu, T. Xu, Y. Ren, et al., On combining visual perception and color structure based image quality assessment. *Neurocomputing*, 212 (2016) 128-134.

[44] X. Cheng, M. Zeng, X. Liu, Feature-preserving filtering with L_0 gradient minimization. *Comput. Graph.* 38 (2014) 150-157.

[45] H. Zhao, Q. Li, H. Feng, Multi-focus color image fusion in the HSI space using the sum-modified-laplacian and a coarse edge map. *Image. Vision Comput.* 26 (9) (2008) 1285-1295.

[46] A. M. Eskicioglu, P. S. Fisher, Image quality measures and their performance, *IEEE Trans. Commun*. 43 (12) (1995) 2959-2965.

[47] Z. Wang, A. Bovik, R. Sheikh, et al., Image quality assessment: from error visibility to structural similarity. *IEEE Trans. Image Processing*, 13(4) (2004) 600-612.